Global POD Modes From PIV Asynchronous Patches

Tirelli, Iacopo ; Grille Guerra, A.; Ianiro, A.; Sciacchitano, A.; Scarano, F.; Discetti, Stefano

DOI
10.55037/lxlaser.21st.88

Publication date
2024

Document Version
Final published version

Published in
Proceedings of the 21st International Symposium on the Application of Laser and Imaging Techniques to Fluid Mechanics

Citation (APA)
Tirelli, I., Grille Guerra, A., Ianiro, A., Sciacchitano, A., Scarano, F., & Discetti, S. (2024). Global POD Modes From PIV Asynchronous Patches. In *Proceedings of the 21st International Symposium on the Application of Laser and Imaging Techniques to Fluid Mechanics* Article 88 LISBON Simposia. https://doi.org/10.55037/lxlaser.21st.88

Full-domain POD modes from PIV asynchronous patches

Iacopo Tirelli[1], Adrián Grille Guerra[2], Andrea Ianiro[1], Andrea Sciacchitano[2], Fulvio Scarano[2], Stefano Discetti[1*]

1: Universidad Carlos III de Madrid, Department of Aerospace Engineering, Madrid, Spain
2: Delft University of Technology, Faculty of Aerospace Engineering, Delft, The Netherlands
* Corresponding author: stefano.discetti@uc3m.es

Keywords: PIV, POD, local asynchronous measurements

ABSTRACT

A method is proposed to obtain full-domain spatial modes based on Proper Orthogonal Decomposition (POD) of Particle Image Velocimetry (PIV) measurements performed at different (overlapping) spatial locations. When performing robotic volumetric Particle Image Velocimetry (PIV) (Jux et al., 2018), the large-scale mean velocity fields are estimated merging several measurements performed at different (adjacent) locations covered by the robot sequence. The proposed methodology leverages the definition of POD modes as eigenvectors of the spatial correlation matrix to obtain also large-scale modes. Performing measurements over overlapping (50-75%) regions allows to approximate the correlation matrix in the two adjacent domains. When applied over a sequence of views, this method has the potential to deliver full-domain POD modes spanning the volume covered by the robot sequence, even if different regions are covered asynchronously. This methodology is particularly well-suited for applications that seek to investigate large-scale flow structures, whenever the dynamic spatial range (DSR) of the measurement system does not allow to capture the whole domain at once. The methodology is validated using a 2D experimental dataset of a turbulent boundary layer, where patches are artificially created from splitting the PIV measurements, later used as ground truth to assess the results. Furthermore, we apply the technique to a 3D robotic volumetric PIV experiment of the flow around a wall-mounted cube.

1. Introduction

Three-dimensional Particle Image Velocimetry (PIV) and Lagrangian Particle Tracking (LPT) are increasingly used for the investigation of complex and unsteady three-dimensional flow fields (Schroeder and Schanz, 2023).

Recent advances in volumetric PIV using helium-filled soap bubbles (HFSB) as flow tracers (Scarano et al., 2015) enable to afford larger measurement domains up to the order of 1 m^3. Nonetheless, measurements in domains with complex geometry and limited optical access are still elusive due to the lengthy procedures associated with system setup and calibration. The recently introduced coaxial volumetric velocimetry (CVV, Schneiders et al. 2018) is well suited for robotic manipulation of the velocimeter that aims to circumvent the problem of optical access by performing several, local, volumetric measurements without the need for recalibration after the repositioning of the probe. This approach has been demonstrated in the work of Jux et al. (2018), where the flow around a full-scale replica of a professional cyclist was surveyed. On the downside, robotic PIV performs independent measurements at each position of the probe, resulting into separated, often partly overlapping, patches (or sub-domains), which prevents the visualization of instantaneous flow scales that exceed the size of an individual measurement region. As a result, flow statistics are obtained by "stitching" measurements performed in independent sub-domains (or patches), assuming ergodicity and measuring at different time instants (asynchronous) in different regions the probability density functions of the velocity fluctuations. However, the partition of the investigated volume in patches prevents the visualization of any instantaneous flow feature that exceed the size of an individual measurement region. In the asynchronous measurements, visualization of instantaneous flow structures with any size larger than that of a patch is only possible under strong assumptions, for instance assuming periodicity of certain phenomena whose phase is either known a-priori or can be obtained from each measured patch. This limitation has hindered, so far, the interpretation of coherent flow structures spanning more than a single patch using, for instance, popular modal analysis techniques such as the Proper Orthogonal Decomposition (POD, Lumley 1967).

In this work, we propose a method that faces the above problem by producing an estimate of the spatial POD modes spanning a domain of interest covered by a multitude of asynchronous measurements, under the assumption that patches always overlap with each other to a certain extent. For this purpose, we leverage the definition of POD spatial modes as eigenvectors of the spatial correlation matrix, obtained through measurements from patches with a certain overlap. Two cases are examined with the proposed method. In Sec.3 we assess the proposed methodology employing a planar PIV measurements dataset of a turbulent boundary layer, where the whole measurement domain is subdivided into patches, in order to simulate the case of asynchronous measurements. The second case deals with an experiment performed using robotic PIV on the flow around a wall-mounted cube.

2. Methodology

The principle of the proposed methodology is graphically exemplified in the flow-chart shown in Figure 1. We assume that instantaneous snapshots of the velocity vector field are obtained asynchronously in different regions of the domain of interest (DOI). The velocity vector may be either computed by spatial cross-correlation or by binning scattered vectors obtained from particle tracking (Agüera et al., 2016). For simplicity, it is assumed that the velocity vectors are available on a global Cartesian grid: $\boldsymbol{x} = (x, y) \in \boldsymbol{R}^{n_x \times n_y}$ in 2D or $\boldsymbol{x} = (x, y, z) \in \boldsymbol{R}^{n_x \times n_y \times n_z}$ for 3D measurements, where n_x, n_y and n_z are the number of grid points along the corresponding directions x, y and z.

The measured dataset is reorganized into a matrix $\boldsymbol{U}$ of dimensions N_p (total number of grid points) and N_t (total number of snapshots). For the case of domains covered with asynchronous measurements in patches, each snapshot will contain information only in the set of points corresponding to the patch for that time instant. Subsequently, the snapshot matrix is composed of the original velocity fields masked by zeros in the region outside of the patch. This can be written as a Hadamard product between $\boldsymbol{U}$ and a Dirac delta function matrix δ, with zeros entries in the locations without velocity information:

$$\widehat{\boldsymbol{U}} = \delta \odot \boldsymbol{U}, \tag{1}$$

where $\odot$ denotes the Hadamard product and $\widehat{\boldsymbol{U}} \in \boldsymbol{R}^{N_p \times N_t}$ represents the masked version of $\boldsymbol{U}$. The spatial correlation matrix $\boldsymbol{C} \in \boldsymbol{R}^{N_p \times N_p}$ is computed from the masked velocity fields and decomposed via Singular Value Decomposition (SVD) as in the following equation:

$$\boldsymbol{C} = \widehat{\boldsymbol{U}}\, \widehat{\boldsymbol{U}}^{\boldsymbol{T}} = \boldsymbol{\Phi\Sigma\Psi^T\Psi\Sigma\Phi^T} = \boldsymbol{\Phi\Sigma^2\Phi^T}, \tag{2}$$

with $\boldsymbol{\Phi} \in \boldsymbol{R}^{N_p \times N_p}$ and $\boldsymbol{\Psi} \in \boldsymbol{R}^{N_t \times N_t}$ the matrices whose columns contains respectively the spatial modes ϕ_i and the temporal modes ψ_i, $\boldsymbol{\Sigma} \in \boldsymbol{R}^{N_p \times N_t}$ the diagonal matrix whose elements σ_i represent the singular values.

The matrix $\boldsymbol{C}$ contains the correlations between the velocities at the different points of the domain. If the patches do not overlap, non-zero entries of $\boldsymbol{C}$ are limited to pairs of points belonging to the same patch; pairs of points belonging to different patches will be assigned a correlation value equal to zero. Instead, if patches overlap, non-zero entries of $\boldsymbol{C}$ are achieved in the overlap regions. This approach effectively extends the correlation information beyond the patch boundary and provides a better approximation of the spatial correlation matrix. To take this into account, each element of the correlation matrix $\boldsymbol{C}$ is divided by the corresponding number of occurrences.

It must be remarked that the use of spatially overlapping patches allows solely the recovery of the global spatial modes and not of the temporal modes. Therefore, the current method should not be regarded as a technique that performs low-order reconstruction of the flow dynamical behavior. For the latter, the patches should not only be overlapping, but they should also feature some temporal overlapping, which brings us to the original problem of a measurement range that simultaneously covers the whole DOI.

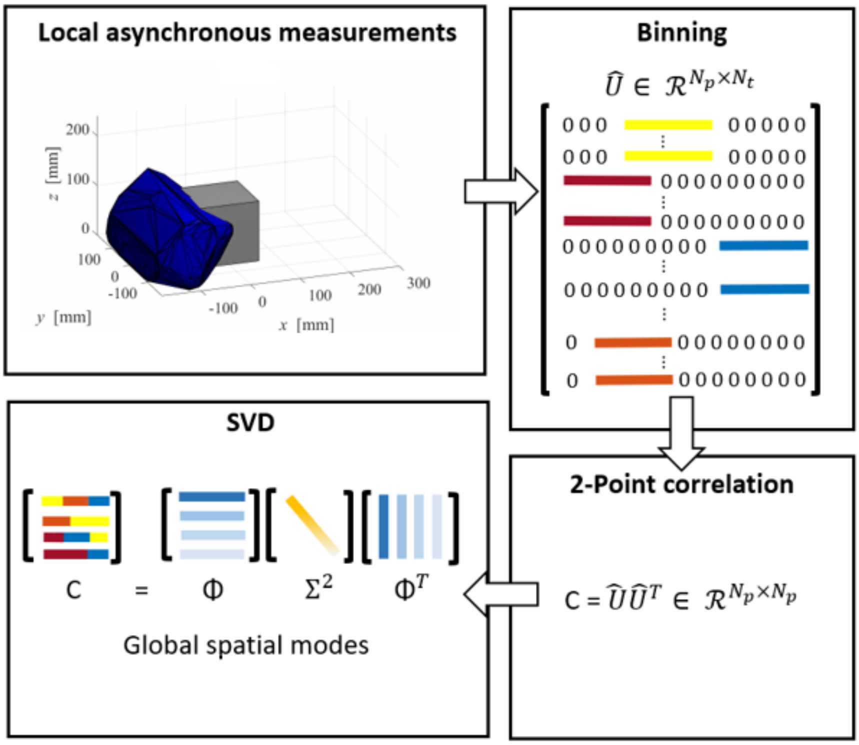

Figure 1. Flowchart of the proposed algorithm.

3.1. Application to planar TBL data

The method is validated here making use of planar PIV measurements of a turbulent boundary layer. The experiments are performed in the wind tunnel facility of the Department of Aerospace Engineering at Universidad Carlos III de Madrid. The experimental setup and measurement procedures are here shortly mentioned. For a full description, the reader is referred to Güemes et al. (2019). Figure 2 depicts the layout of the experiment: the flow develops along a smooth methacrylate flat plate (3) measuring 1.25 meters in length and 10 millimeters in thickness, it extends the full height of the wind tunnel and is positioned 0.09 meters away from the nearest wind tunnel wall. In Tab 1 the main boundary layer parameters are reported, evaluated at $x = 0.875$ m: free-stream velocity U_∞, wall-friction velocity u_τ, boundary layer thickness δ_{99}, displacement thickness δ^*, the Reynolds numbers Re_τ and Re_θ (based respectively on wall-friction velocity u_τ and momentum thickness θ) and the shape factor H_{12}.

Table 1. Experimental parameters at x = 0.875 m.

$U_\infty [m/s]$	u_τ [m/s]	δ_{99} [mm]	δ^* [mm]	Re_τ	Re_θ	H_{12}
15.5	0.64	24.7	3.7	1040	2800	1.36

Illumination is provided by a dual cavity Ng:YAG Quantel Evergreen laser (1), whose illumination region starts from $x = 0.875$m. The flow is seeded with droplets of Di-Rthyl-Hexyl-Sebacate (DEHS) generated by a Laskin nozzle. An Andor Zyla sCMOS 5.5 MP (2) has been used to capture PIV images with a resolution of 48500 pix/m. A Quantum composer 9520 Series Pulse Delay Generator has been employed to coordinate illumination and recording. Other specifics about the experimental setup are reported in Tab. 2.

Table 2. Specifics of the experimental setup.

Flow facility	Göttingen-type wind tunnel. Test section: 0.4 m x 0.4 m x 1.5 m. Velocity range: 4 m/s to 20 m/s. Turbulence intensity below 1%.
Seeding	Laskin nozzle. Droplets of Di-Rthyl-Hexyl-Sebacate (DEHS) with d = 1μm.
Illumination	Dual cavity Ng:YAG Quantel Evergreen laser 200 mJ/pulse at 10 Hz.
Imaging	Andor Zyla sCMOS 5.5 MP (2560 × 2160) pixel array, 6.5 × 6.5 μm pixel size, resolution 48500 pix/m. Objective Tokina 100 mm lens. $f_{\#} = 16$.
Post-processing	POD background removal (Mendez et al 2017), iterative multi-grid/multi-pass algorithms (Willert and Gharib (1991) and Soria (1996)), image deformation (Scarano 2001), B-spline interpolation (Astarita and Cardone (2005) and Astarita (2007)).

Specific database settings can be found in the work by Tirelli et al. (2023) and accessed openly at https://zenodo.org/records/6922577. A total number of 39,000 snapshots is acquired, covering a DOI of 40 x 40 mm^2. The baseline for the validation of the algorithm is obtained with cross-correlation with a final interrogation window of 32 × 32 pixels (0.06 x 0.06 mm^2) and an overlap factor of 50%. The data analysis is carried out over the entire domain simultaneously. Later, the snapshots are partitioned into rectangular subdomains, i.e. the patches, as depicted in Figure 2: the blue patch is an example of a patch close to the border, while the yellow and the black ones are examples of the largest patches in the middle of the domain. The maximum patch size is $\delta_{99} \times \delta_{99}$, that corresponds to 80 × 80 vectors on a total number of 120 × 120 gridpoints. The overlap among patches is set to 75%. The patched snapshots are built by extracting the velocity vectors from a random selection of the PIV dataset (without repetition) and then masked according to the patch location in the domain. This configuration leads to a total of 36 patches that cover the entire domain.

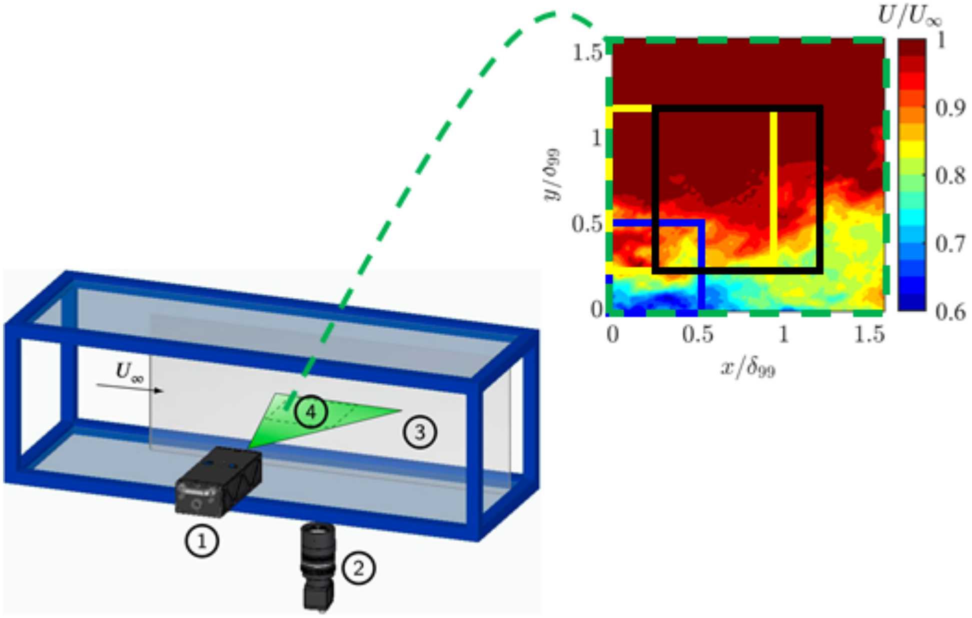

Figure 2. Sketch of the experimental setup adapted by Tirelli et al 2023. The magnification of the camera field of view depicts the streamwise velocity contour of the TBL. Examples of patches (composed of 80x80 vectors) with 75% overlap are shown as yellow and black frames. The blue frame is an example of patch on the boundary (in this case, composed only of 20x20 vectors).

The global POD spatial modes obtained following the strategy discussed in the previous section are reported in the top part of Figure 3 (where the corresponding mode number is highlighted in black). The coordinates are normalized to the local boundary layer thickness δ_{99}. To establish a ground-truth, a POD analysis of the entire DOI is performed, and the spatial modes are reported on the bottom of the same figure (highlighted in blue). We limit the discussion here to the first twelve spatial modes φ_i, scaled with the square root of the total number of points N_p. Given the chaotic nature of the turbulent motions, the energy spectrum is relatively flat and these 12 modes account for approximately 70% of the total energy of fluctuations.

The first two modes appear to be accurately captured. Furthermore, up to the 5th mode, the topology of the fluctuation is well reproduced. Although, the reconstruction does reproduce the modes as from the reference data, the following inconsistencies are noticed: 1) the mode rank is occasionally shifted (e.g. mode 8 from the reconstruction corresponds to mode 9 in the reference data); 2) in some cases the mode is represented with inverted sign (e.g. mode 9 from the reconstruction and mode 8 from the reference). In this type of analysis, achieving perfect synchronization in time and sign of the modes is challenging due to differences in input datasets and the varying scales that the method can recover, leading to distinct decompositions. Furthermore, subtle differences in the energy content might shuffle modes with similar energy content.

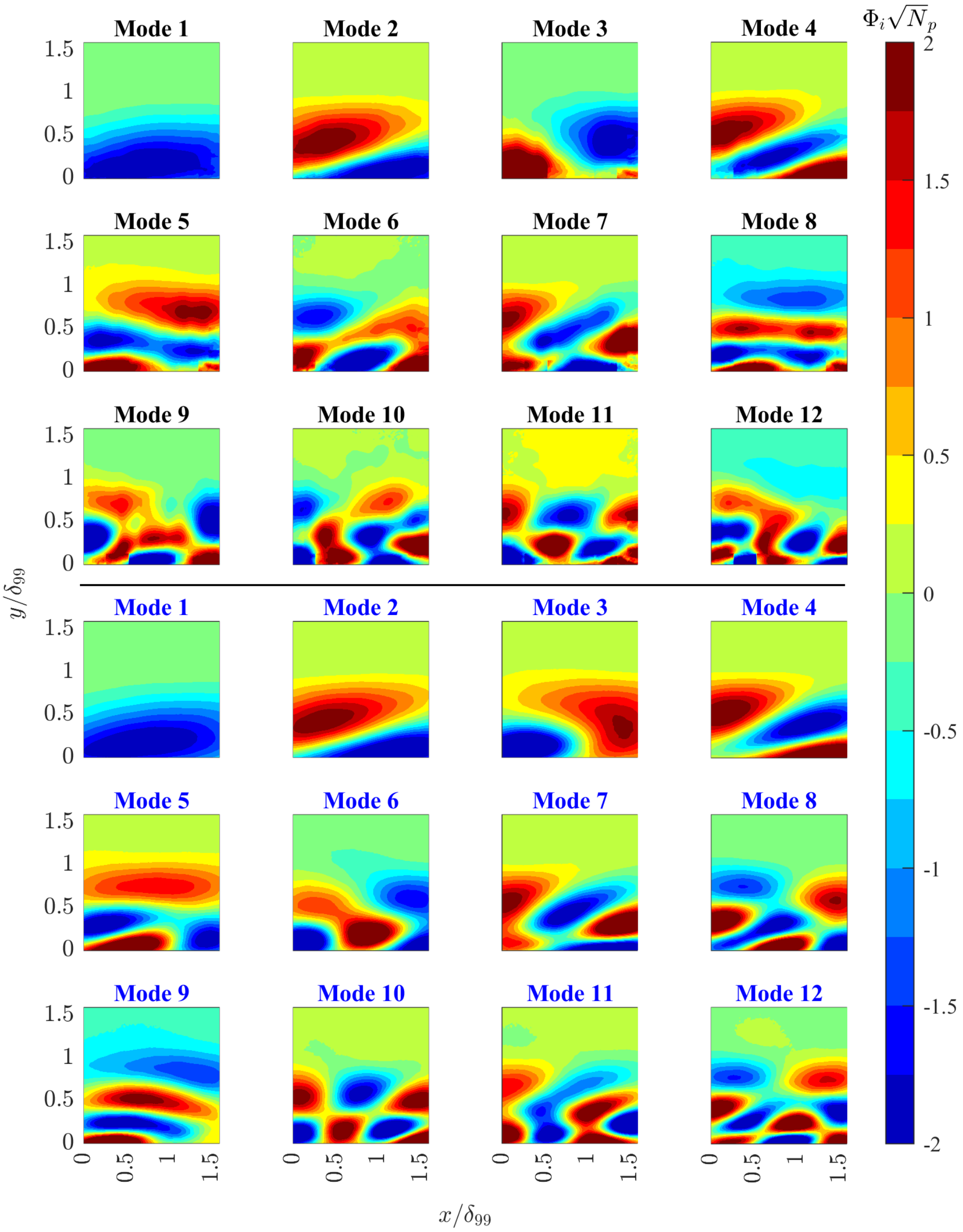

Figure 3. Contour plot of the streamwise velocity component of the first twelve POD spatial modes ϕ. Top side (black): modes from the patched dataset. Bottom side (blue): modes from the PIV dataset.

In Figure 4 the eigenvalue distributions obtained employing the two methodologies are presented: the result of the patched approach is depicted with black dots, while the reference with a blue continuous line. The energy associated to each mode is normalized using the total energy of the whole DOI POD. The two distributions appear to exhibit a good agreement, with a maximum discrepancy of 10% for the third mode. This further confirms the observations made regarding the spatial modes.

Interestingly enough, the spatial modes presented in Figure 3 can be linked to the coherent features present within a turbulent boundary layer. The first modes are indicative of the large-scale motions present in the outer part of the boundary layer, given their significant energy

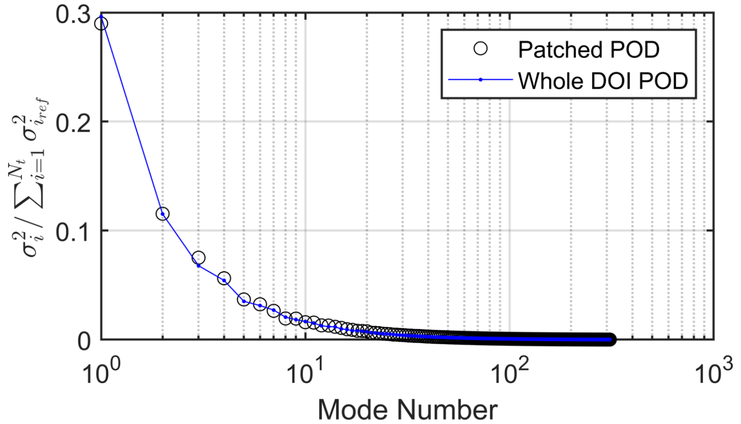

Figure 4. Eigenvalue distribution for Patched POD (black circle) and whole DOI POD (blue continuos line) normalized with the total amount of energy of the reference case (whole DOI POD).

content. Building upon the insights from the work of Sanmiguel Vila et al. (2017), a similar physical interpretation of the patterns revealed by the first spatial modes can be provided. Modes one and three appear to be coupled: the first one is representative of a sweep/ejection process (Wallace 2016) while the third mode represent a phase-quadrature event that models the convection of low/high momentum coherent motions inside and outside the measurement domain. The same consideration holds for mode two and four which are representative of a shear layer behaviour.

3.2. Modal reconstruction from 3D patches

Experimental validation involves the study of the flow around a wall-mounted cube, whose side D measures 12 cm. The 3D patches have been extracted using Robotic PIV. Large-aperture three-dimensional Lagrangian Particle Tracking measurements with 7 cameras imaging the full domain has been used as a reference. Both experimental campaigns were conducted at the TU Delft Aerodynamics Laboratories in an open-jet, open-circuit, low-speed wind tunnel (W-tunnel). The freestream velocity U_∞ is set at 10 m/s, that corresponds to a Reynolds number $Re = 81{,}000$.

HFSBs were used as tracer particles. The HFSBs seeding generator comprises 10 parallel wings, each 1 meter in span and equipped with 20 nozzles spaced 5 cm apart. This setup results in a seeding rake with a total of 200 nozzles, covering a seeding surface area of approximately 0.95 × 0.50 m^2 in the wind tunnel's settling chamber. The generator, operated by a LaVision fluid supply unit, controls the pressure of air, helium, and soap, which are set at 2.0, 1.5, and 2.0 bar, respectively. The nominal diameter of the tracer particles is 300 μm.

The two experimental setups are sketched in Figure 5. The robotic system velocimeter probe consists of four CMOS cameras equipped with an objectives of 4 mm focal length, integrated within

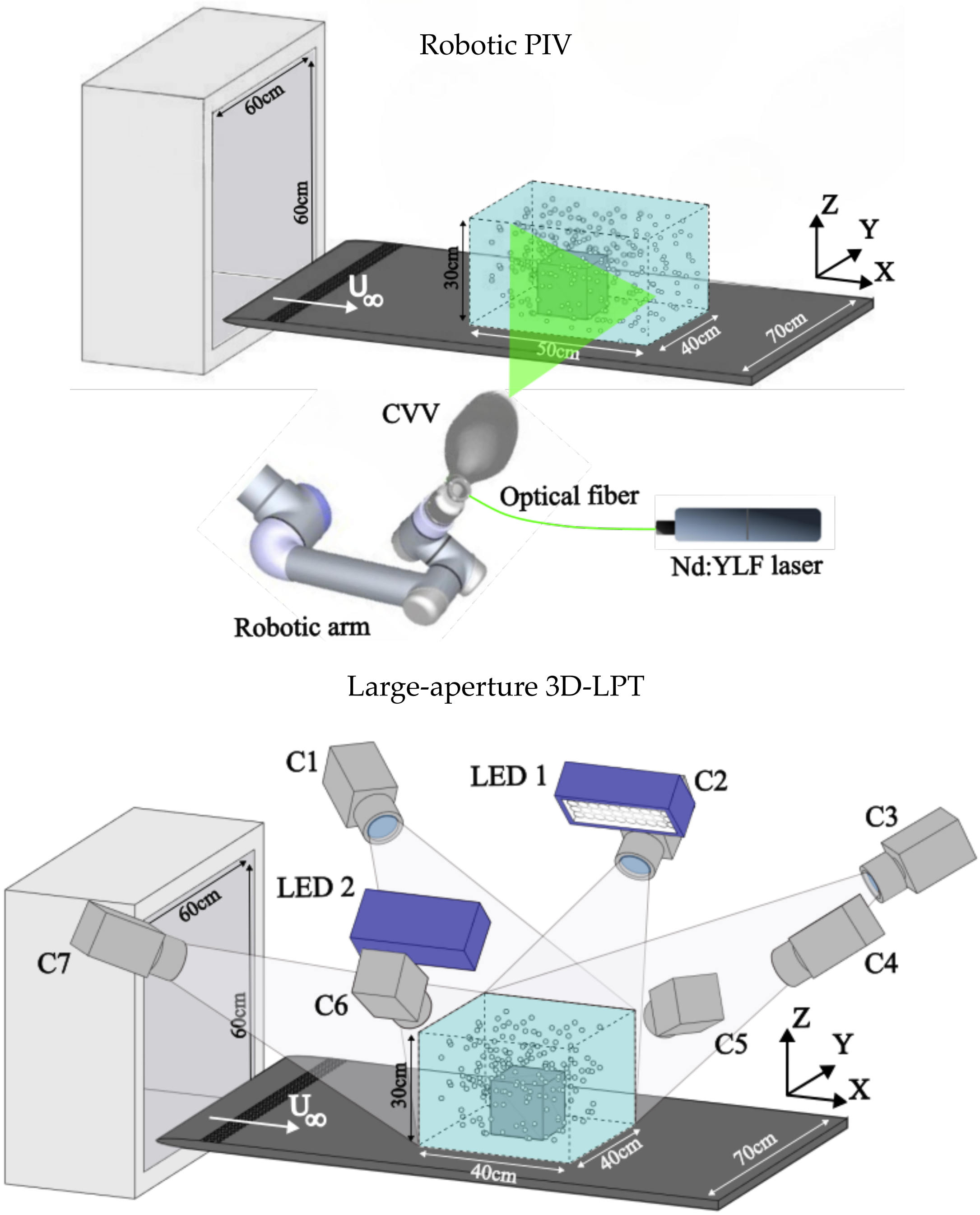

Figure 5. Sketch of the two experimental setups: on top the robotic PIV, on bottom the large-aperture 3D-LPT (Hendriksen et al. 2024).

the LaVision MiniShaker Aero. The illumination of the investigated domain is provided by a Quantronix *Darwin Duo* Nd:YLF diode-pumped laser ($\lambda = 527$ nm, 2 × 25 mJ pulse energy at 1 kHz). A total of 35 patches with high overlap (5000 snapshots each) has been acquired with an acquisition frequency of 200 Hz. The patches cover an investigation region spanning $x \in [-180,300]$ mm, $y \in [-180,180]$ mm and $z \in [0,240]$ mm. The size of each patch is approximately 200 mm. For further details about the robotic system, the reader is referred to Kim et al. (2020). The acquired images are then analyzed using the two-pulse Shake-The-Box algorithm with predictor.

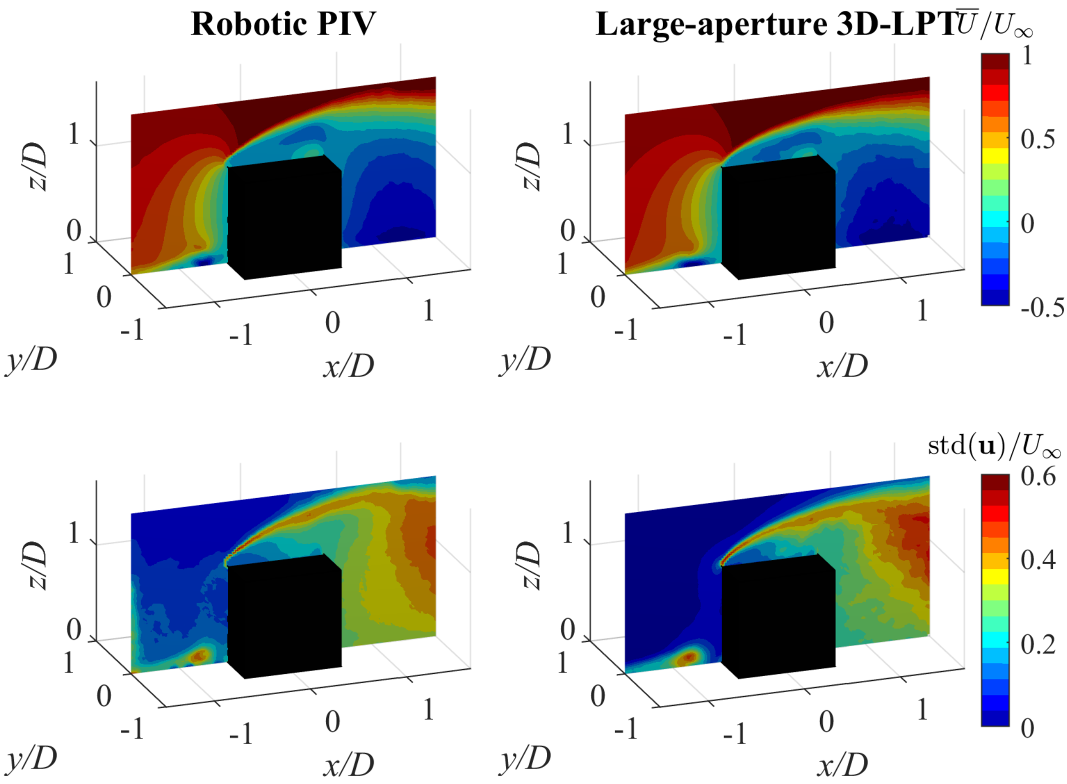

Figure 6. On top ensemble average using top-hat averaging at b = 10 mm while on the bottom standard deviation of the velocity magnitude, on the left the patched case while on the right the reference one. Both normalized with the freestream velocity U_∞.

The experimental setup of the large-aperture 3D-LPT experiments used as reference is detailed in the work of Hendriksen et al. (2024). For this measurement 7 high-speed CMOS camera were used while the illumination was provided by two LEDs. A total amount of 10000 snapshots (two independent sequences of 5000 snapshots each) were acquired at a frequency of 3 kHz. The investigated domain in this case has the same spanwise and wall-normal extension as in the robotic-PIV experiment, but a shorter streamwise extension ($x \in [-180, 200]\ mm$).

To perform a fair comparison between the results of the two measurements, all the data are binned onto the same grid ($x/D \in [-1.5D, 1.67D]$, $y/D \in [-1D, 1D]$ and $z/D \in [0D, 1.67D]$) with a bin size of $D/3$ (or 4 cm) and 75% overlapping.

In Figure 6 the flow statistics of the two methodologies, both normalized with the freestream velocity U_∞, are compared. The top panel shows the ensemble averages obtained through top-hat averaging with a bin size of 10 mm, while the bottom panel displays the standard deviations of the velocity magnitude, on the left the patched case while on the right the reference ones.

These statistics highlight that despite the same observed phenomena and experimental conditions, the two techniques exhibit different levels of accuracy, which can lead to variations in the results.

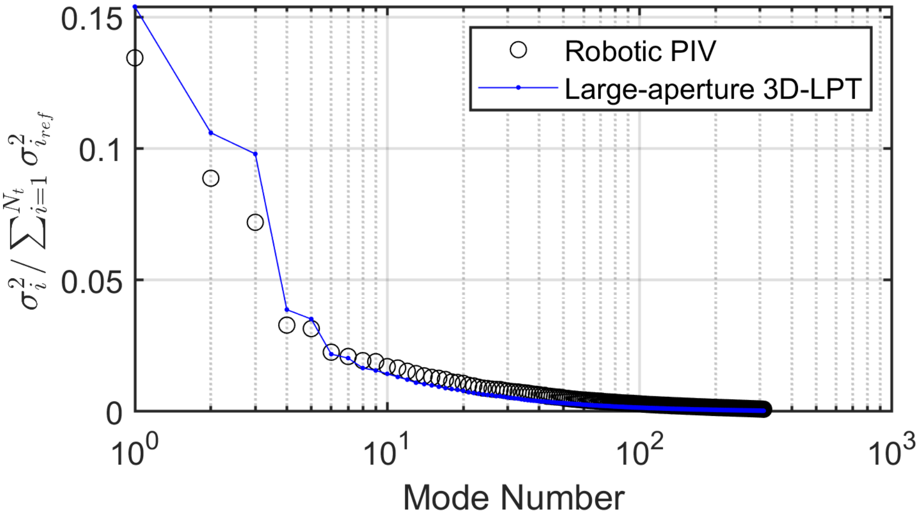

Figure 7. Eigenvalue distribution for Robotic PIV (black circle) and large-aperture 3D-LPT (blue continuous line) normalized with the total amount of energy of the reference case (large-aperture 3D-LPT).

The RoboticPIV is limited in terms of resolution if compared to the large-aperture 3D-LPT, primarily due to the different arrangement (in terms of number, sensitivity and resolution of cameras), to the lower tomographic aperture and to the co-axial direction between imaging and illumination (Schneiders et al., 2018).

Figure 7 presents the eigenvalue distributions for both cases, normalized with the total amount of energy from the large-aperture 3D-LPT measurements case. In this representation, the black line depicts the Robotic PIV results, while the blue line represents the reference large-aperture 3D-LPT data. The figure illustrates that the robotic reports a lower energy level in the modes. This is to be ascribed to the truncation of the spatial correlation due the finite size of the patch.

A comparison among the first 5 spatial modes in terms of vortical structures is presented. The widely used Q-criteria (Hunt et al.1988) is employed in this study to highlight the coherent structures described by the modes. The value of Q for the i-th mode is computed from the dimensionless quantity $\phi_i \sigma_i / U_\infty$.

As reported in the study by da Silva et al. (2024), common features of all surface-mounted finite-height square prisms include the horseshoe vortex and the arch vortex, followed by dipole/quadrupole vortical structures in the wake. Their position, strength, and behavior are primarily dependent on the aspect ratio (AR) of the prism, boundary layer thickness (δ/D), and the Reynolds number (Re) investigated.

For the specific case of the cube, which can be considered a prism with $AR = 1$, the main structure is the arch vortex (Martinuzzi and Tropea, 1993). This structure is easily recognizable by the presence of two legs, where the flow rotates around wall-normal (vertical) axes, and a roof, where the rotation is around a horizontal axis perpendicular to the free-stream direction. The experimental study of this vortex was carried out by Becker et al. (2002), while Kawai et al. (2012)

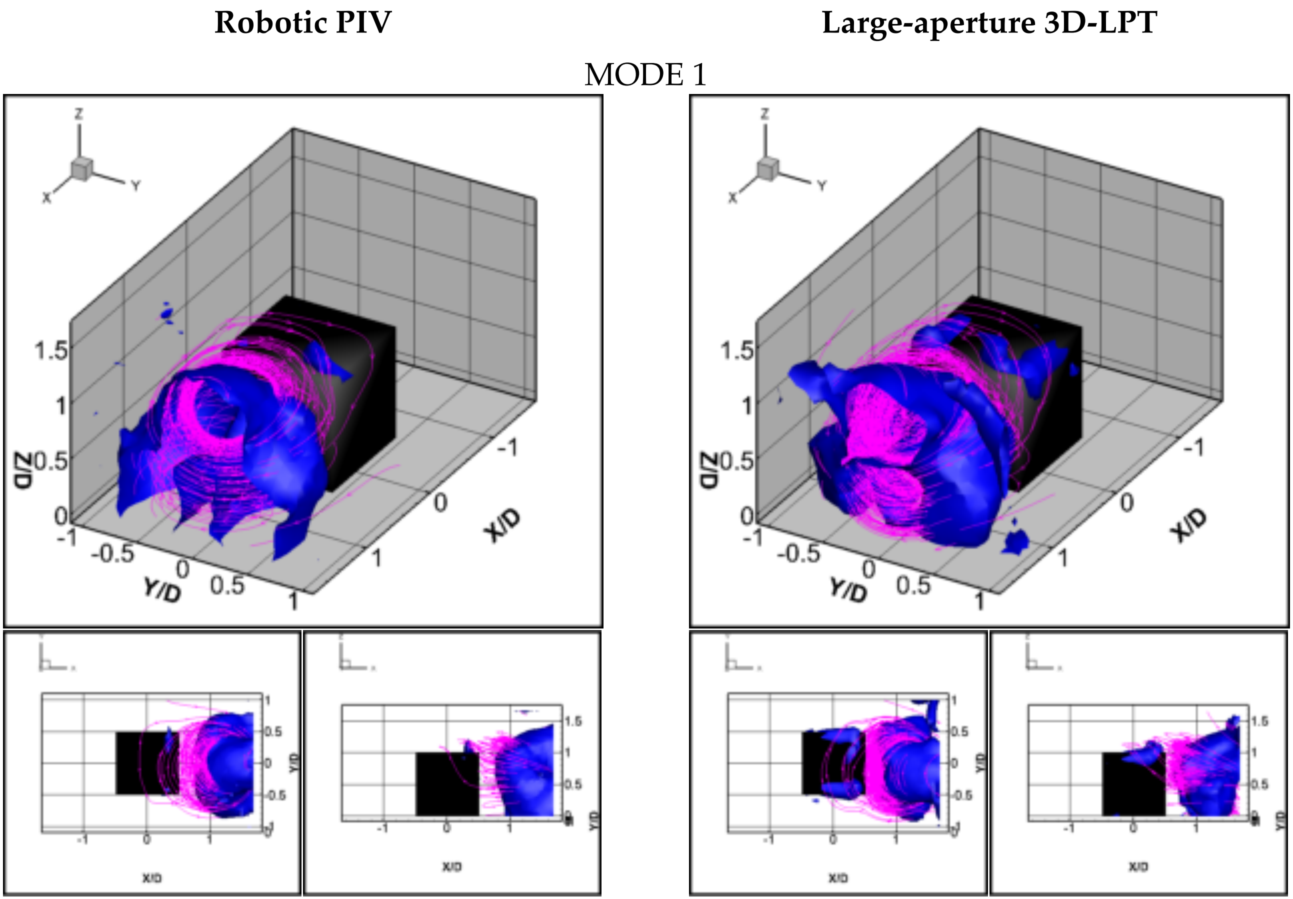
Robotic PIV

Large-aperture 3D-LPT

MODE 1

Figure 8. Positive Q visualization for the spatial mode 1: on the left RoboticPIV while on the right the large-aperture 3D-LPT. The associated streamlines are depicted in magenta.

captured the temporal evolution of this vortex using stereoscopic PIV (SPIV), revealing characteristics similar to the von Kármán street.

Figure 8 depicts the vortical structures associated with the first spatial mode. This mode appears to describe the vortex core behind the arch, as confirmed by the magenta streamlines. The limitations of the robotic PIV, compared to the reference, are particularly evident in the region near the cube. The reference mode highlights edge vorticity that the robotic PIV failed to capture. Nonetheless, the shape of the structure identified by the RoboticPIV is overall consistent with the one described by the first mode of the full-domain large-aperture 3D-LPT.

Figure 9 shows the modes 2 and 3 which seem to be in phase quadrature, describing a streamwise displacement of the arch vortex. In the second mode, the arch is visible with both methodologies, supported by a vortex. The only difference is that the reference mode exhibits a hole in the roof and appears closer to the cube. In the third mode, the situation is reversed: the mode from the robotic PIV misses part of the roof while the reference one is complete. This time, the legs of the arch are not aligned, suggesting that the coupled modes together describe the "shedding" of the

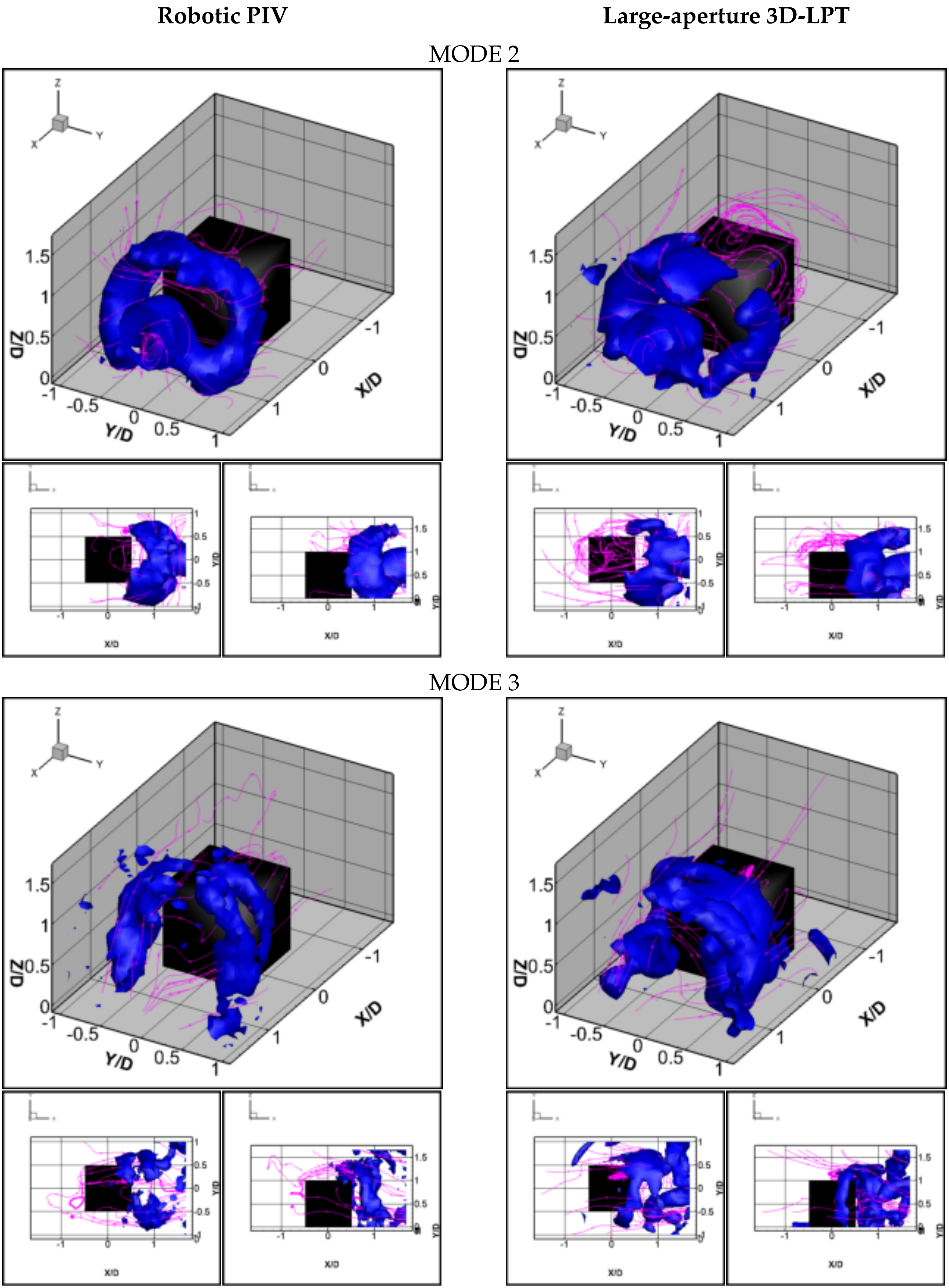

Figure 9. Positive Q visualization for the spatial mode 2 and 3: on the left RoboticPIV while on the right the large-aperture 3D-LPT. The associated streamlines are depicted in magenta.

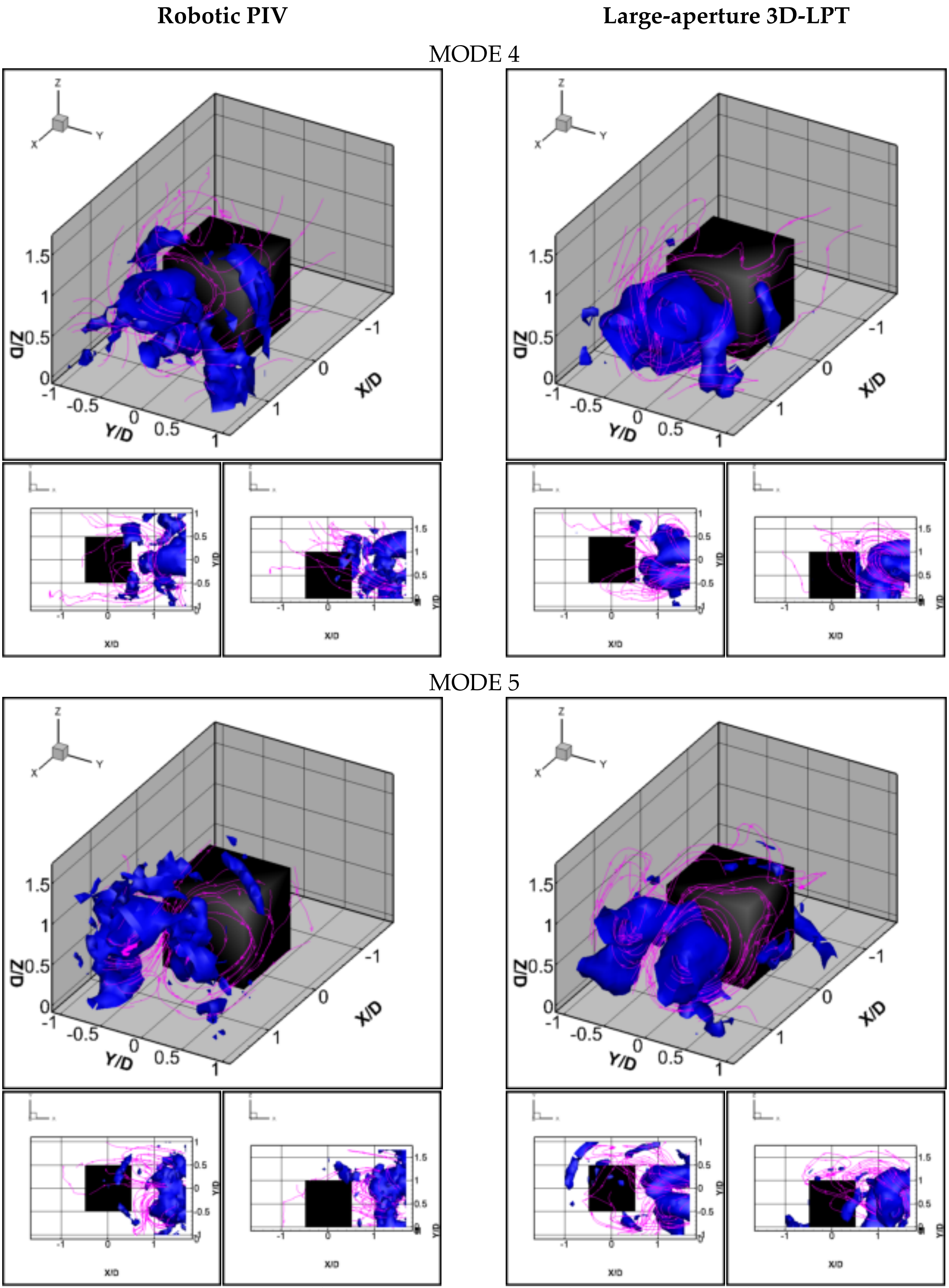

Robotic PIV

Large-aperture 3D-LPT

MODE 4

MODE 5

Figure 10. Positive Q visualization for the spatial mode 4 and 5: on the left RoboticPIV while on the right the large-aperture 3D-LPT. The associated streamlines are depicted in magenta.

arch. Another significant discrepancy, linked to the difference in resolution, is the vortex cluster behind the arch in the reference case, which is missed by the robotic PIV.

A second couple of modes (4-5) are reported in Figure 10. Here, a dipole-type wake is highlighted with a phase quadrature between the consecutive modes. Other notable structures are the trailing edge vortices close to the cube. In the mode 5 from the reference experiment, a horseshoe vortex is well captured, while it is not well observed in the corresponding robotic mode. Overall, however, there is a very satisfactory matching in the structure of the identified modes, thus supporting the validity of our approach to obtain full-domain modes from patches.

4. Conclusions

A methodology to achieve full-domain POD spatial modes starting from asynchronous measurements in different flow regions of a domain is proposed. The technique is based on computing the two-point correlation matrix, forcing some overlap between patches to maximize the number of computed terms of the matrix. The eigenvectors of the correlation matrix approximate the global spatial modes. The main target of this method are large-scale measurements, where it is often necessary to collect data in patches of the domain to have a global picture of the flow field, like in the Robotic PIV.

A validation has been carried out by dissecting 2D measurements of a turbulent boundary layer in patches. The POD modes obtained with our method using solely the patches match reasonably well with the results of a modal decomposition run on the entire domain. An application to a volumetric robotic PIV experiment on the flow around a wall-mounted cube has been also carried out. The results show a good agreement between the modes identified by merging asynchronous patches and those obtained by a large-aperture 3D-LPT covering the entire domain. This approach opens the possibility of obtaining global modes on a larger scale than the volume observed by each realization.

Acknowledgments

This project has received funding from the European Research Council (ERC) under the European Union’s Horizon 2020 research and innovation program (grant agreement No 949085, NEXTFLOW ERC StG). Views and opinions expressed are however those of the authors only and do not necessarily reflect those of the European Union or the European Research Council. Neither the European Union nor the granting authority can be held responsible for them.

References

Astarita, T. (2007). Analysis of weighting windows for image deformation methods in PIV. *Experiments in fluids, 43, 859-872.*

Astarita, T., & Cardone, G. (2005). Analysis of interpolation schemes for image deformation methods in PIV. *Experiments in fluids, 38, 233-243.*

Becker, S., Lienhart, H., & Durst, F. (2002). Flow around three-dimensional obstacles in boundary layers. *Journal of Wind Engineering and Industrial Aerodynamics, 90(4-5), 265-279.*

da Silva, B. L., Sumner, D., & Bergstrom, D. J. (2024). Revisiting the surface-mounted cube: An updated perspective of the near wake and near-wall flow field. *International Journal of Heat and Fluid Flow*, *106*, 109288.

Güemes, A., Ianiro, A., & Discetti, S. (2019). Experimental assessment of large-scale motions in turbulent boundary layers. *In 13th International Symposium on Particle Image Velocimetry.*

Hendriksen, L.A., Sciacchitano, A., Scarano, F. (2024). Object registration techniques for 3D-PIV/LPT. *21st Int. Symp. on Applications of Laser and Imaging Techniques to Fluid Mechanics. Lisbon Portugal.*

Hunt, J. C., Wray, A. A., & Moin, P. (1988). Eddies, streams, and convergence zones in turbulent flows. Studying turbulence using numerical simulation databases, 2. *Proceedings of the 1988 summer program.*

Jux, C., Sciacchitano, A., Schneiders, J. F., & Scarano, F. (2018). Robotic volumetric PIV of a full-scale cyclist. *Experiments in Fluids, 59, 1-15.*

Kawai, H., Okuda, Y., & Ohashi, M. (2012). Near wake structure behind a 3D square prism with the aspect ratio of 2.7 in a shallow boundary layer flow. *Journal of wind engineering and industrial aerodynamics, 104, 196-202.*

Kim, D., Kim, M., Saredi, E., Scarano, F., & Kim, K. C. (2020). Robotic PTV study of the flow around automotive side-view mirror models. *Experimental Thermal and Fluid Science*, *119*, 110202.

Lumley, J. L. (1967). The structure of inhomogeneous turbulent flows. *Atmospheric turbulence and radio wave propagation, 166-178.*

Martinuzzi, R., & Tropea, C. (1993). The flow around surface-mounted, prismatic obstacles placed in a fully developed channel flow (data bank contribution).

Mendez, M. A., Raiola, M., Masullo, A., Discetti, S., Ianiro, A., Theunissen, R., & Buchlin, J. M. (2017). POD-based background removal for particle image velocimetry. *Experimental Thermal and Fluid Science, 80, 181-192.*

Sanmiguel Vila, C., Örlü, R., Vinuesa, R., Schlatter, P., Ianiro, A., & Discetti, S. (2017). Adverse-pressure-gradient effects on turbulent boundary layers: statistics and flow-field organization. *Flow, turbulence and combustion, 99, 589-612.*

Scarano, F. (2001). Iterative image deformation methods in PIV. *Measurement science and technology, 13(1), R1.*

Scarano, F., Ghaemi, S., Caridi, G. C. A., Bosbach, J., Dierksheide, U., & Sciacchitano, A. (2015). On the use of helium-filled soap bubbles for large-scale tomographic PIV in wind tunnel experiments. *Experiments in Fluids, 56, 1-12.*

Schneiders, J. F., Scarano, F., Jux, C., & Sciacchitano, A. (2018). Coaxial volumetric velocimetry. *Measurement Science and Technology, 29(6), 065201.*

Schröder, A., & Schanz, D. (2023). 3D Lagrangian particle tracking in fluid mechanics. *Annual Review of Fluid Mechanics, 55, 511-540.*

Soria, J. (1996). An investigation of the near wake of a circular cylinder using a video-based digital cross-correlation particle image velocimetry technique. *Experimental Thermal and Fluid Science, 12(2), 221-233.*

Tirelli, I., Ianiro, A., & Discetti, S. (2023). An end-to-end KNN-based PTV approach for high-resolution measurements and uncertainty quantification. *Experimental Thermal and Fluid Science, 140, 110756.*

Wallace, J. M. (2016). Quadrant analysis in turbulence research: history and evolution. *Annual Review of Fluid Mechanics, 48, 131-158.*

Willert, C. E., & Gharib, M. (1991). Digital particle image velocimetry. *Experiments in fluids, 10(4), 181-193.*